Nanoscale

PAPER

View Article Online
View Journal | View Issue



Cite this: *Nanoscale*, 2025, **17**, 3973

# The intriguing role of L-cysteine in the modulation of chiroplasmonic properties of chiral gold nano-arrows†‡

Nada Khalfaoui-Hassani,[a] Mary Tabut,[a,b] Ndeye Haby Awe,[a] Christophe Desmarets,[c] Daniele Toffoli,[d] Mauro Stener,[d] Nicolas Goubet,*[a] Monica Calatayud *[a,b] and Caroline Salzemann *[a]

Developing chiral plasmonic nanostructures represents a significant scientific challenge due to their multidisciplinary potential. Observations have revealed that the dichroic behavior of metal plasmons changes when chiral molecules are present in the system, offering promising applications in various fields such as nano-optics, asymmetric catalysis, polarization-sensitive photochemistry and molecular detection. In this study, we explored the synthesis of plasmonic gold nanoparticles and the role of cysteine in their chiroplasmonic properties. Specifically, we synthesized chiral gold nano-arrows using a seed-mediated-growth synthesis method, in which gold nanorods are used as seeds while incorporating L-cysteine into growth solution as a chiral ligand. Our results show clearly that the chiral molecule transfers chirality to gold nanocrystals and the morphology is controlled through kinetic growth. In addition, we demonstrate that the chiroplasmonic properties, such as the sign of circular dichroism, can be modulated using only one enantiomeric form in the growth solution. To understand the origin of such an effect, we conducted theoretical modelling using density functional theory. Our results point to the intermolecular cysteine interactions as a key factor in the dichroic properties of surface-molecule chiral systems.

Received 7th October 2024,
Accepted 23rd November 2024

DOI: 10.1039/d4nr04131c

rsc.li/nanoscale



## Introduction

Chirality is defined by an absence of symmetry that causes objects with this feature to differ from their mirror image. Due to such a feature, objects with a chiral morphology, called enantiomorphs (EMs), interact differently in a chiral environment. In particular, one of the main characteristics of chirality is the specific optical response to circularly polarized electromagnetic radiation (right or left).[1] Plasmonic nanocrystals (NCs), due to their increased interaction with light *via* localized surface plasmon resonance (LSPR) excitation, exhibit enhanced chiroptic properties.[2] In this context, one of the current challenges in the nanoscience community is the development of novel chiral plasmonic nanostructures because of their multidisciplinary potential in fields such as nano-optics, asymmetric catalysis, polarization-sensitive photochemistry and molecular detection.[1,3,4] Plasmonics has been a fertile ground for discoveries and innovation, because metallic nanostructures act as nano-antennas, by coupling to incoming electromagnetic radiation and concentrating its radiant energy, thereby promoting the conversion of light into other forms of energy.[5] In this context, efforts have been devoted to developing different strategies for producing chiral plasmonic nanostructures.[1,3,6,7] So far, systems with high dissymmetry factors are manufactured using physical routes that created the field of chiral plasmonics, which aims to control near and far-field chiroptical responses.[8] Nevertheless, these techniques are expensive and have a low output. It is therefore necessary to develop new ways to fabricate chiral metallic nanoparticles.

Among the alternative synthesis methods, colloidal chemistry is a promising way due to its versatility in controlling the final nanomorphology. The latter is determined by a set of thermodynamic (reduction potentials, surface passivation,

[a]*Sorbonne Université, MONARIS, CNRS-UMR 8233, 4 Place Jussieu, F-75005 Paris, France. E-mail: nicolas.goubet@sorbonne-universite.fr, caroline.salzemann@sorbonne-universite.fr*
[b]*Sorbonne Université, CNRS, Laboratoire de Chimie Théorique, LCT, 4 Place Jussieu, F-75005 Paris, France. E-mail: monica.calatayud@sorbonne-universite.fr*
[c]*Sorbonne Université, IPCM, CNRS-UMR 8232, 4 Place Jussieu, F-75005 Paris, France*
[d]*Department of Chemical and Pharmaceutical Sciences, University of Trieste, 34127 Trieste, Italy*

†Electronic supplementary information (ESI) available. See DOI: https://doi.org/10.1039/d4nr04131c.

‡Theoretical calculations available, see DOI: https://doi.org/10.17172/NOMAD/2024.12.05-2 (datasets.dataset_name = CHIRNATIO - Cluster 92 AMS) DOI: https://doi.org/10.17172/NOMAD/2024.12.05-3 (datasets.dataset_name = CHIRNATIO - Cluster 78 AMS). The experimental data are available in Recherche Data Gouv (see https://doi.org/10.57745/1ECSSF).

temperature, *etc*.) and kinetic (concentration, mass transport, temperature, *etc*.) parameters that are intimately and intrinsically linked to each other.[9] One of the great interests in seed mediated growth synthesis is that nucleation and growth steps are physically separated which allows tuning both thermodynamic and kinetic parameters.[9] This provides chemists with wider possibilities to drive the crystal growth toward a specific morphology. In the literature, the elaboration of chiral NCs often employs thiolated molecules such as cysteine as a strong chirality imprinter, inducing surface modification or formation of a chiral shell.[10–12] In this context, the asymmetric shape control in order to obtain metallic enantiomorphs with an intrinsic chiral morphology remains very challenging. In 2018, Lee *et al.* obtained for the first time gold helicoidal NCs by seed mediated growth from cubic and octahedral seeds.[13] Since then, few groups have elaborated on nanoparticles with a chiral morphology such as gold propellers and octopods.[14–16] Recently, A. Carone *et al.* have reported the elaboration of chiral gold nanoparticles from five-fold bipyramids characterized by high-index Miller indices.[10] They have shown that chiral molecules entrapped in the gold bipyramids induce chiral properties. In 2023, Liz-Marzán *et al.* obtained chiral twisted nanorods exhibiting high-index facets.[17]

Until now, the mechanisms of formation of chiral gold nanocrystals and the origin of their optical activity have not been well understood and theoretical studies are needed to complete the experimental observations. Govorov *et al.* have described theoretically the chirality transfer from a chiral molecule to an achiral plasmonic nanoparticle. From their study, it appears that the chiro-plasmonic response of a hybrid system can be explained by near-field dipolar interactions for a nanoparticle size lower than the wavelength excitation. For a bigger size (larger than 100 nm), the quasi-static approximation cannot be applied and the circular dichroism (CD) signal is due to the long-range electrodynamics mechanism.[18–20] More recently, Morales-Vidal *et al.* proposed for the first time a description close to the experimental systems of the chirality transfer in gold nanoparticles by L-cys considering density functional theory (DFT) simulations.[17,21] In addition to molecule–nanoparticle systems, static DFT and TD-DFT simulations have been reported to explore the quantum-mechanical origin of chiroptical properties of pure gold chiral nanostructures (*i.e.* without a chiral molecule).[22]

In this context, our approach is to elaborate plasmonic gold enantiomorphs by seed mediated growth. The main challenge is to break the face cubic centered fcc symmetry of the bulk gold crystal. To this, we use as seeds single crystalline nanorods (NRs) with an aspect ratio of up to 5 characterized by a reduced symmetry, which are further grown by a favored kinetic process in the presence of a chiral molecule. In the present article, we report the synthesis of gold nanoarrows by the seeding process from gold NRs in the presence of L-cys. We provide evidence that the chiral morphology can be kinetically controlled by the concentration of L-cys in the growth solution. An unexpected modulation of their chiroplasmonic properties is observed through an inversion in the sign of the CD spectra depending on the concentration of the chiral ligand. TD-DFT simulations support that the intermolecular interaction of the L-cys molecules at the metallic surface of the nanoparticles could be the origin of such behavior.

# Experimental

### Chemical elaboration of chiral gold nano-arrows

**The gold nanorods** used as seeds are first synthesized in a two-step process considering a protocol already established.[23] First of all, small 2 nm spherical nanoparticles are obtained by taking a mixture of 5 mL of CTAB (100 mmol $L^{-1}$) and 5 mL of $HAuCl_4{\cdot}3H_2O$ (1 mmol $L^{-1}$) into a 50 mL flask under magnetic stirring at room temperature. Next, 0.95 mL of $NaBH_4$/NaOH (10 mmol $L^{-1}$) is introduced into the reaction medium. The solution rapidly changes color from yellow to brown, characteristic of the formation of 2 nm seeds (Fig. S1A†). In the second step, 20 mL of CTAB (100 mmol $L^{-1}$) and 20 mL of $HAuCl_4{\cdot}3H_2O$ (1 mmol $L^{-1}$) are introduced into a bottle of 50 mL. Then, 0.88 mL of $AgNO_3$ (10 mmol $L^{-1}$) and 2 mL of hydroquinone (100 mmol $L^{-1}$) are introduced, and in the end, 50 μL of 2 nm seed solution are added. The solution is incubated in a thermostatic bath at 30 °C for 12 h. After the reaction, a dark brown solution is obtained showing the formation of gold nanorods. Finally, the solution is washed through centrifugation for 5 h at 30 °C with a speed of 5500 rpm to recover the nanoparticles (Fig. S1A†).

**The chiral gold nano-arrows** are obtained by the kinetic growth of the previously synthesized nanorods (Fig. S1B†). To a 20 mL flask, 4.66 mL of CTAC (17 mmol $L^{-1}$) and 0.2 mL of $HAuCl_4{\cdot}3H_2O$ (3 mmol $L^{-1}$) are mixed under magnetic stirring. Next, a volume of 0.088 mmol $L^{-1}$ of $AgNO_3$ (3 mmol $L^{-1}$) is introduced into the reaction mixture.

It seems important to note that cysteine is characterized by three acid functions: a carboxylic group ($pK_a$ = 1.9), a mercapto group ($pK_a$ = 8.1) and an amino group ($pK_a$ = 10.2). Hence, for the pH range of 1.9–8.1, cysteine presents a zwitterionic form ($NH_3^+ - SH - COO^-$). In order to lower the aggregation of nanoparticles stabilized by L-cysteine through electrostatic interactions, it is necessary to consider a pH lower than 1.9. However, the redox potential of hydroquinone is pH dependent which means that working at a low pH drastically increases its redox potential, which is not in favor of kinetic growth and thus of the breaking symmetry needed for obtaining enantiomorphs.[9] It is therefore necessary to consider a compromise between the redox potential and electrostatic interactions by fixing the pH to 1.8. Hence, the pH is adjusted by adding 1 mol $L^{-1}$ of HCl to 1.9. 5 μL of L-cysteine solution at different concentrations of 1, 3 and 10 mmol $L^{-1}$ is further added. This corresponds to a total concentration of cysteine in the growth solution of 0.9, 2.7 and 9.1 μmol $L^{-1}$ respectively. Then, 0.475 mL of a mild reducing agent (hydroquinone) is added. A change in the color of the solution from yellow to colorless is observed, which is characteristic of the reduction of $Au^{3+}$ to $Au^+$. Finally, 0.05 mL of solution containing $1 \times 10^{-9}$

 

mol $L^{-1}$ of the previously synthesized nanorods is added. The reaction is maintained at 30 °C for 2 h. After the reaction, the solution is centrifuged for 30 min at 30 °C at a speed of 6000 rpm to recover the nanoparticles. The colorless supernatant is discarded, and the precipitate is redispersed in 1 mmol $L^{-1}$ to prevent aggregation.

### Characterization

**Electron microscopy.** We used a Hitachi SU-70 Field Emission Scanning Electron Microscope at 15 kV for obtaining SEM-FEG images. The colloidal solution is evaporated on an immersed silicon wafer.

For conventional transmission electron microscopy, we used a JEOL 1011 at 100 kV, whereas for high resolution, we used a JEOL 2100+ at 200 kV. The grids were prepared by drop-casting a concentrated solution of nanocrystals dispersed in water.

**Circular dichroism spectroscopy.** CD spectra were recorded on a Jasco J-815CD spectrometer with a 1 mm path-length quartz cell. Measurements were conducted either under synthesis conditions *in situ* or directly two hours after the reaction. The displayed absorption spectra result from subtraction of the spectrum of the standard solvent solution (water). Spectra were recorded in the wavelength range 900–400 nm for all attempts with a scan speed of 100 $nmin^{-1}$ at 20 °C for two accumulations.

**Raman spectroscopy.** 50 μL of a concentrated solution of nano-arrows solubilized in 1 mmol $L^{-1}$ of CTAB were deposited on a gold mirror and left until complete evaporation of the solvent before proceeding with the measurements. Raman spectroscopy measurements were performed using a HE785 spectrometer from HORIBA Jobin Yvon. The measurement interface is a SuperHead probe that incorporates an edge filter for Rayleigh filtering and is coupled to the spectrometer and the laser source at 785 nm by optical fibres. The measurement is carried out using a long working distance 40× infrared microscope objective. The laser power on the sample was adjusted to approximately 100 mW.

**UV visible spectroscopy.** UV visible absorption spectra in the range of 250 and 1200 nm were acquired for all samples with a VARIAN Cary 5000 spectrometer.

### DFT and TD-DFT simulations

**DFT calculations.** The Vienna *Ab initio* Simulation Package (VASP 6.4.0)[24,25] was used to conduct calculations at the density functional theory (DFT) level. A plane-wave basis set with a cutoff of 450 eV was employed to depict the valence electrons of Au, S, H, C, O, and N atoms (corresponding to 11, 6, 1, 4, 6, and 5 valence electrons, respectively).[25] Simultaneously, the core electrons were treated using projector-augmented wave (PAW) pseudopotentials.[26] The PBE exchange–correlation functional was utilized,[27] and van der Waals corrections[28] were introduced through the Grimme D3 approach.[29] For simulating the Au(111) surface, periodic boundary conditions were employed, involving four atomic layers. During the DFT optimization, the bottom two layers remained fixed to mimic the bulk, while the top two Au layers were allowed to fully relax. We also applied a dipole correction along the *z*-axis and maintained a 15 Å vacuum region between the slabs. The studied Au facet was described as $p(4 \times 4)$ slabs, and the Brillouin zone was sampled for all models using a 3 × 3 × 1 *k*-point mesh generated *via* the Monkhorst–Pack method.[30] The creation of cluster models was facilitated using VESTA (Visualization for Electronic and Structural Analysis) version 3.5.8.[31]

**TD-DFT calculations.** The CD spectra of the selected clusters were calculated using the complex-polarizability TDDFT method,[32,33] an efficient damped linear response implementation of the TDDFT equations included in the AMS package[34,35] together with the B3LYP hybrid xc-functional[36,37] treated within the hybrid-diagonal approximation (HDA).[38,39] HDA affords an efficient method to use the hybrid xc-functional within TDDFT when using Slater-type basis functions, whereby only the diagonal elements of the RPA matrix of linear response TDDFT include the non-local Hartree–Fock exchange of the full xc kernel while treating all the non-diagonal terms at the simpler adiabatic LDA level. Recent works have showcased the accuracy and efficiency of the method, giving results in very good agreement with those corresponding to the full hybrid kernel at a fraction of the computational cost.[38,39] All calculations have been performed at the scalar relativistic level within the zero-order relativistic approximation (ZORA)[40] in order to include relativistic effects, which are important for heavy elements such as gold. A Slater Type Orbital (STO) basis set of Triple Zeta plus Polarization (TZP) quality has been employed for all atomic fragments of L-cysteine and for all Au atoms of the first layer in close proximity to the adsorbate, while an STO-DZ basis set was used for all remaining Au atoms of the finite cluster models.

Circular dichroism is defined as the difference between the absorbance of left and right circularly polarized light. For an electronic transition from the ground state $|0\rangle$ to the *n*-th excited state $|n\rangle$ and assuming a random orientation of the sample, as is usual for experiments in solution, it can be expressed as:

$$CD = \frac{4}{3}\gamma \,\mathrm{Im}(\langle 0|\boldsymbol{\mu}|n\rangle \cdot \langle n|\boldsymbol{m}|0\rangle) = \frac{4}{3}\gamma R_{0n} \quad (1)$$

where $\gamma$ is a constant factor and $\boldsymbol{\mu}$ and $\boldsymbol{m}$ are the electric dipole and the magnetic dipole moment, respectively. $R_{0n}$ is the rotatory strength (in units of $10^{-40}$ $esu^2$ $cm^2$), which enters in the following sum-over-states expression for the diagonal elements of the optical rotation tensor $\beta$:

$$\bar{\beta} = \frac{1}{3}\sum_u \beta_{uu} = \frac{2c}{3}\sum_n \frac{R_{0n}}{{\omega_{0n}}^2 - \omega^2} \quad (2)$$

where the sum is over the complete set of excited electronic states of the system, $\omega$ is the photon energy and $\omega_{0n}$ is the excitation energy corresponding to the $|0\rangle \rightarrow |n\rangle$ electronic transition. Within polTDDFT, the CD spectrum is obtained from the imaginary part of $\beta$ (see ref. 32 and 33 for a detailed derivation of the relevant equations). CD spectra are calculated for

photon energies with an imaginary part of $\omega_i$ = 0.060 eV, which leads to a Lorentian broadening of the profiles with the same half-width at half-maximum (HWHM).

## Results and discussion

The main difficulty in the elaboration of gold nanoparticles with a chiral morphology is the high symmetry related to the fcc structure. Hence, it is necessary to find strategies to significantly decrease or break the symmetry.

Since 2018, several publications have demonstrated that the growth of gold nanocrystals in the presence of L-cys induces both a dichroism signal and a change in morphology. This is due to its selective adsorption on certain facets, which can grow in such a way to induce asymmetrical geometries.[13,41] The choice of such amino acid is motivated by the presence of a thiol function, which is well known to have strong affinity to the gold surface and can then assure its anchoring at the seed surface.

In our study, we considered the seeding growth from nanorods used as seeds in a growth solution containing different concentrations of L-cys (Fig. S1†). The synthesis of single crystalline gold NRs has been intensely reported in the literature.[42–47] Their synthesis and characterization studies are detailed in the *Experimental* section and in Fig. S2.†

In the absence of L-cys, the SEM-FEG image shows the formation of gold nano-arrows (Fig. 1a). These objects can be described by two square pyramidal heads and four extruded facets forming a cross-body with a concave shape. They have an average length of 69 ± 6 nm and a width of 30 ± 3 nm that corresponds to an aspect ratio of almost 2.3 ± 0.4 which is significantly lower compared to that of initial seeds which is 6. This is clearly confirmed by UV-visible spectroscopy (Fig. S3†). Indeed, the optical spectrum obtained after the growth exhibits both a red-shift of the T-LSPR transverse band from 506 to 575 nm and a blue-shift of the L-LSPR longitudinal band from 930 to 731 nm. In order to obtain chiral nanoparticles, the same growth was performed for different concentrations of L-cys from 0 to 9.1 μmol $L^{-1}$ (Fig. S4†). At a low concentration of 0.9 μmol $L^{-1}$, we observed the formation of nano-arrows similar in size and shape to those obtained without L-cys (Fig. 1b). As the concentration was increased to 2.7 μmol $L^{-1}$ and 9.1 μmol $L^{-1}$, crystal enantiomorphs were obtained. For these higher concentrations, some morphological evolutions of the nano-arrows were progressively observed (Fig. 1c and d).

The chiroptical characterization of each sample was performed by circular dichroism and is displayed in Fig. 2 and Fig. S4.† As expected, in the absence of L-cys, no CD signal is observed (black curve). For 0.9 μmol $L^{-1}$, even though no morphological changes are observed, the corresponding CD spectrum exhibits a negative Cotton effect around 600 nm, giving evidence of a chiral behavior (red curve). Surprisingly, by increasing the concentration to 2.7 μmol $L^{-1}$ and 9.1 μmol $L^{-1}$, the CD spectra exhibit a positive Cotton effect (blue and green curves). Fig. S4d† shows the plot of the intensity of the

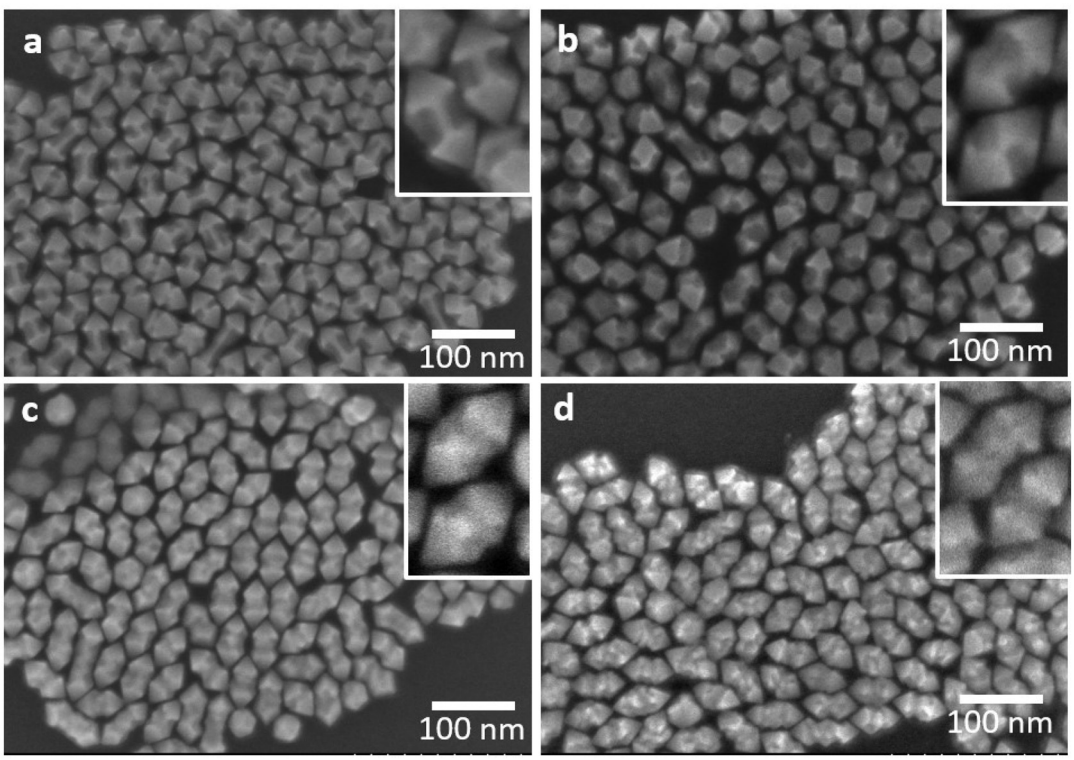


**Fig. 1** SEM-FEG images of gold nano-arrows obtained from seed mediated growth at different concentrations of cysteine for (a) 0 μmol $L^{-1}$, (b) 0.9 μmol $L^{-1}$ (c) 2.7 μmol $L^{-1}$ and (d) 9.1 μmol $L^{-1}$ of cysteine.

 

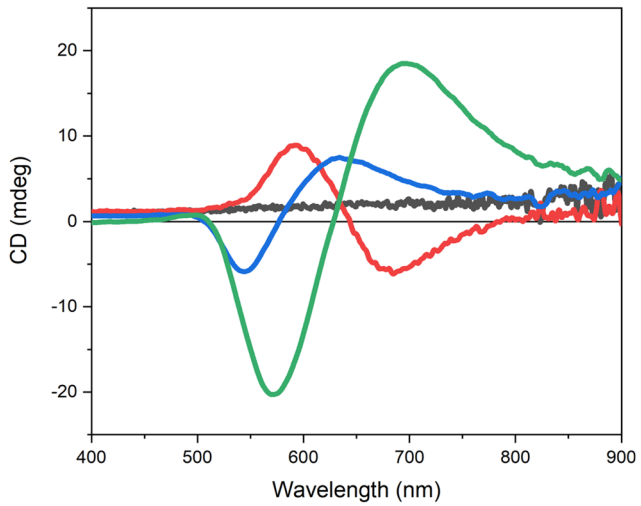


**Fig. 2** Circular dichroism spectra corresponding to nano-arrows obtained in the absence (black) and in the presence of 0.9 μmol $L^{-1}$ (red), 2.7 μmol $L^{-1}$ (blue) and 9.1 μmol $L^{-1}$ (green) of L-cysteine.

CD signal at a lower wavelength, we see that the inversion occurs for concentrations between 0.91 and 2.7 μmol $L^{-1}$. This result is somehow unexpected as L-cys is used in both syntheses and all experimental parameters are the same except for the concentration of the molecule.

Considering that L-cys alone has a CD signal in the UV region, around 180 nm, the CD signal around 600 nm is attributed to the adsorbed L-cys at the metallic surface. Indeed, such a hybrid system defined by a chiral molecule at the surface of achiral plasmonic nanoparticles has been described and studied by Govorov *et al.*[18–20] They showed that for a hybrid molecule–nanoparticle system, both an enhancement of the chiral molecule's signal and a modification of the structure of its spectrum are observed. This is explained by the presence of the chiral molecule that generates a chiral dissipative electric current within the nanoparticle, due to coulombic interactions between the molecule and the metallic nanoparticle. This leads to the appearance of an induced plasmon at the LSPR wavelength. In other words, the plasmon becomes chiral.

Experimentally, the anchoring of L-cys was confirmed by Raman spectroscopy. The spectrum obtained in the absence of the chiral molecule (Fig. S5a†) exhibits an intense band at 160 $cm^{-1}$ corresponding to the metallic atom Au–Au vibrations and others between 800 and 1500 $cm^{-1}$ that are related to the amine and ammonium functions of the surfactant ($CTA^+$, cation from CTAB and CTAC). In the presence of L-cys (Fig. S5b–d†), even at low concentrations, we can observe an additional band at 270 $cm^{-1}$ which is characteristic of the Au–S vibration. We can note that on the one hand, the intensity of the Au–S band increases with the increase in the concentration. On the other hand, the bands between 800 and 1500 $cm^{-1}$ are better defined for higher concentrations of the molecule, which could be related to a SERS effect of the cysteine at the surface.

The intriguing point concerning our results is that L-cys, used for all samples, can induce different chiroptical signatures. This observation is not an artifact. Indeed, the same behavior is observed for growth performed considering D-cysteine, an enantiomer of L-cysteine (Fig. S6,† dashed line). For all concentrations, the CD signals are inverted comparatively to those obtained with L-cys. In this case, an inversion from a positive Cotton effect to a negative one by increasing the concentration can be noticed. This observation confirms that L(D)-cysteine is responsible for the chiral behavior but cannot explain the inversion observed by increasing the concentration.

At this point, we have gold nanoparticles surrounded by L-cys that have different chiroptical properties. A possible effect of chiral morphology on the dichroism signal inversion cannot be excluded. According to the high-resolution SEM images (Fig. 1), a double-arrow morphology is always obtained whatever the concentration of L-cys introduced. However, the morphology evolves.

To understand the morphological evolution of gold nanocrystals, high-resolution TEM was performed (Fig. 3). At a low amount of L-cys (0.9 μmol $L^{-1}$), the nanoarrows are identical in size and shape to those obtained in the absence of cysteine (Fig. S7†). The HRTEM image confirms that arrows are single crystalline (Fig. 3a). Indeed, the crystallographic planes extended on the overall crystal. The heads are composed of

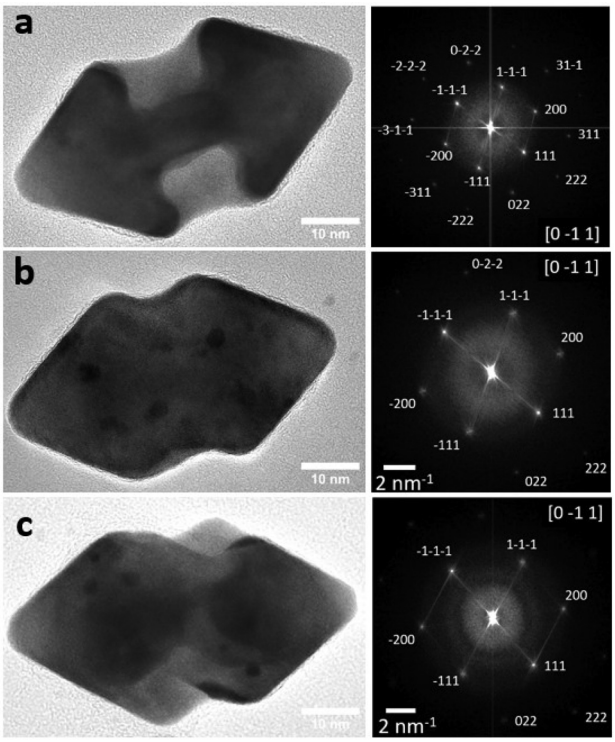


**Fig. 3** Structural characterization of gold nano-arrows obtained with (a) 0.9 μmol $L^{-1}$, (b) 2.7 μmol $L^{-1}$ and (c) 9.1 μmol $L^{-1}$ of L-cysteine. HRTEM images and the corresponding calculated FFT on the overall HRTEM image.

four {111} facets truncated at the tip by the {100} facets and the lateral extruded facets are {110}, leading to the formation of four symmetrical lateral wings (Fig. S7a†).[48] They are characterized by a ratio S/V around 0.27. The {110} and {111} facets represent almost 41% and 59% of the total surface, respectively (Fig. S8†). As we can see on the calculated Fast Fourier Transform, arrows lie on the substrate on the {110} facets as it corresponds to an [0–11] orientation (Fig. S7a†). Our observations are consistent with similar arrows already reported and described by Wang *et al.*[49]

At this concentration, L-cys does not affect the growth. Hence, the CD signal is directly related to L-cys at the gold surface and not to the morphology. When the concentration is increased to 2.7 μmol $L^{-1}$, the morphology is different (Fig. 3b). The lateral concave facets gradually disappear by being filled up. Hence the {110} facets are less and less present while the {111} facets appear at the base of the tips. At a higher concentration (9.1 μmol $L^{-1}$), we see that the {110} facets have completely disappeared, while those of {111} have continued to grow. We observe a "zig-zag" morphology with mostly {111} facets (Fig. 3c). We can clearly see that the additional planes grow asymmetrically from the vertices of the square base of the tips.

To better understand the impact of L-cys on the morphological distortion of gold NCs and its role in modulating chiroptical properties, a functionalization experiment of achiral nanoarrows was carried out. We synthesized gold nanoarrows using hydroquinone in the absence of the chiral ligand (Fig. S7†). After synthesis, different concentrations of L-cysteine were introduced into the nanoarrows redispersed in 1 mmol $L^{-1}$ of CTAB. The mixture was left for 12 h. From the TEM images (Fig. S9†), contrary to previous observations, we can clearly see that the morphology did not evolve. CD spectra show a nearly zero signal at 9.1 μmol $L^{-1}$, which vanishes upon decreasing the cysteine concentration. Raman spectroscopy was performed, and the spectra confirmed the absence of the Au–S signal for 0.9 μmol $L^{-1}$ while a shoulder, which could correspond to Au–S, is observed at a higher concentration (Fig. S9e†). This observation supports the fact that L-cys does not bind to the surface after the growth. In fact, the post-functionalization of achiral arrows by cysteine seems extremely limited by the presence of both CTAB and CTAC at the surface. Hence, to obtain an intense chiroptical signal, it is necessary to bring both gold and L-cys to the surface of the seeds. This is consistent with the observations of Carone *et al.*[10] as well as with Govorov's *et al.* predictions, which show by calculation that the most intense system signal would be one made up of a chiral dielectric core and a plasmonic shell.[20] It is also important to note that the morphology is related to the L-cys concentration at the surface. Both cysteine concentration and morphology are interdependent parameters.

The main question remains about the relationship of chiroptical inversion and the morphology. Are these inversions related to the difference in the morphology, and in such a case, do we have a transition between arrows and "zig-zag" particles during the growth by increasing the concentration? In 2022, Sun *et al.*[50] studied the chiroptical behavior of bichiral plasmonic nanoparticles obtained with cysteine-phenylalanine that have two stereogenic centers. A reversible CD signal can be observed depending on the reducing agent, capping surfactant and Au precursor concentrations. In this study, an evolution of the chiral morphology is observed during the growth leading to a CD signal inversion. More recently, in 2024, Chen *et al.* have performed single-particle circular differential scattering on chiral gold nanocubes (CGNCs). They have investigated the chiroptical responses of the individual CGNCs supported by different substrates (Au, $SiO_2$ and $Au/Al_2O_3$) under the excitation of circularly polarized light. They gave evidence that the optical chirality of CGNCs having the same morphology and handedness is inverted and enhanced when the substrate is changed from $SiO_2$ to Au. This is explained by the modulation of the dielectric properties of the substrate.[51]

In order to understand the evolution of our system, we carried out kinetic monitoring by both UV-visible spectroscopy (Fig. S10†) and CD (Fig. 4) at low and high concentrations of L-cysteine. The nanocrystal growth has been monitored for 240 min. The acquisition time for one spectrum is about 4.5 min, and a spectrum has been recorded every 8 min. We reported in Fig. 4a the evolution with time of the extremum of intensity (mdeg) corresponding to the CD peak at a higher wavelength. In addition, the full spectra are shown in Fig. 4b and c for 9.1 μmol $L^{-1}$ and 0.9 μmol $L^{-1}$, respectively. The arrows illustrate the evolution in time of the intensity, which is consistent with the UV-Visible evolution (Fig. S10†).

Initially, the CD spectrum of the growth solution in the absence of nanorods is flat in the visible range corresponding to a 0 in intensity. As soon as we introduced the nanorods, directly into the quartz cuvette containing the previous growth solution, a first spectrum is recorded at $t_0$ (arrows in 4a). The evolution of intensity is then reported for 9.1 μmol $L^{-1}$ (black) and 0.9 μmol $L^{-1}$ (red) of L-cys. We can clearly see that as soon as the nanorods were added into the solution, a low-intensity, non-zero dichroism signal appeared. Its position corresponds to the RPSL-transverse of the nanoparticles that indicates the adsorption of cysteine at the metallic surface to form a hybrid system at the origin of the CD signal. A progressive increase in signal intensity is observed with time. The most interesting feature is that the CD signal at $t_0$ presents a positive or negative Cotton-effect for high and low concentrations of L-cys respectively as soon as we add the nanorods.

To characterize a possible shape evolution during the reaction, TEM has been performed on nanoparticles extracted from the growth solution at different reaction times corresponding to 10 min, 30 min, 60 min and 120 min after the seed addition (Fig. S11†). At low concentrations, as soon as the seeds are added, the solution turns light pink. The extracted nanoparticles obtained after 10 min exhibit the same nanoarrow morphology similar to those in the absence of L-cys. The morphology does not change over time (Fig. S11$a_x$†). This is consistent with the absence of evolution of the intensity and position of the absorption and CD bands after 10 min (Fig. 4c

 

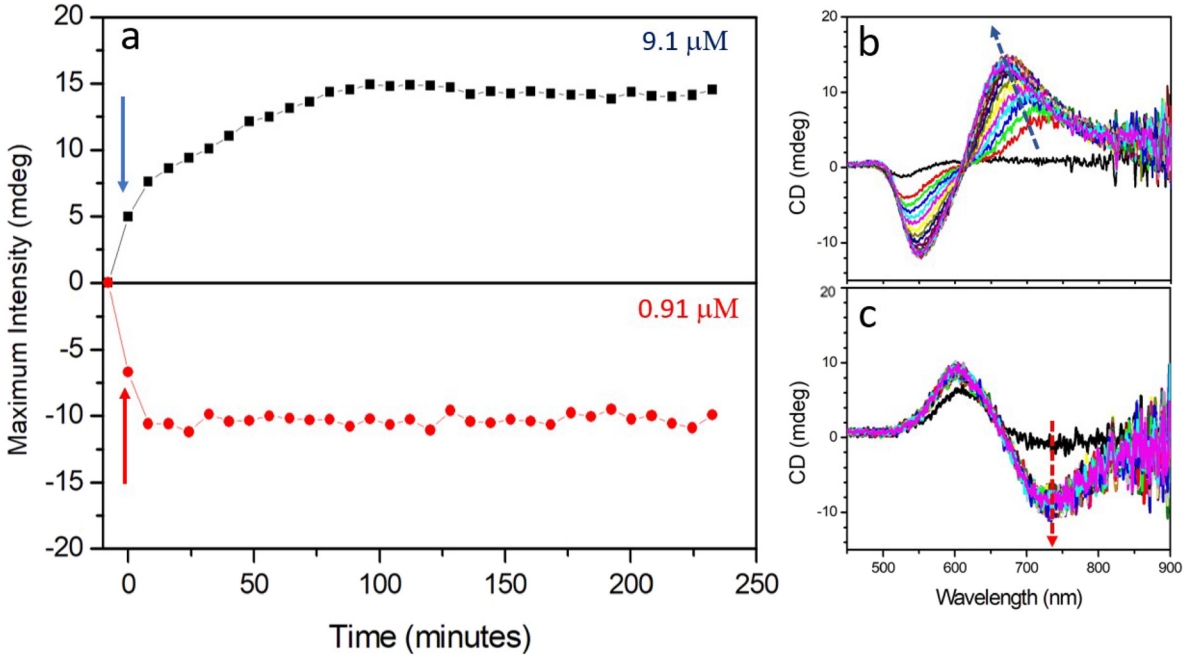


**Fig. 4** Kinetics of the growth followed by circular dichroism. (a) Evolution of the maximum of intensity of the Cotton effect at a higher wavelength with time from the seed addition ($t_0$, marked by arrows) to $t_f$ = 240 min in the presence of 9.1 μmol $L^{-1}$ (black) and 0.9 μmol $L^{-1}$ (red) of cysteine and (b) and (c) the corresponding spectral evolution.

and Fig. S10c†). Conversely, at higher concentration, the kinetics is slower. The solution turns pink 30 min after the seed addition and a blue shift is observed on the UV-Visible and CD spectra, which indicates an evolution in the aspect ratio (Fig. 4b and S10d†). After 40 min, there is no more evolution. From TEM images, 10 min after the seed addition thin nanoarrows with some spikes on their lateral side are observed (Fig. S11$b_1$†). The evolution toward the zig-zag particles occurs in time leading to a decrease of the aspect ratio (Fig. S11$b_x$†).

From the kinetics, we clearly see that for both concentrations, there is no signal inversion during the growth. Furthermore, the kinetics of growth and then the morphology of the nanoparticles in the first 10 min are clearly induced by the L-cys concentration. Both parameters (concentration and morphology) are interdependent.

So, considering that the nanorods are strictly the same (same batch) and that the growth solutions differ only by the L-cys concentration, it is reasonable to assume that this inversion of chiroptic properties depends on L-cys binding and/or its conformation to the surface of the nanorods depending on its concentration. Indeed, relying once again on the study by Govorov, which shows that depending on the orientation of the dipole moments of chiral molecules on the surface, a signal inversion can be observed, we considered the eventuality of L-cys modifications at low and high concentrations. Note that at the working pH, pH = 1.9 ≈ p$K_{a,1}$, we have around 50% of the zwitterionic form, $HSCH_2CH(NH_3^+)(COO^-)$ in our medium. In addition, increasing the concentration may increase intra-molecular interactions.

To emphasize the effect of the concentration in the signal inversion, the same growth has been performed considering another chiral molecule, glutathione, at 0.91, 2.7 and 0.91 μmol $L^{-1}$. As we can see in Fig. S12,† conversely to L-cys, the morphology of the nano-arrows does not change with the concentration. However, a signal inversion is still observed between the lower and higher concentrations. From the CD spectra, 2.7 μmol $L^{-1}$ of glutathione seems to correspond to the transition with a nearly zero signal. These observations confirmed the effect of concentration on the signal inversion conversely to the morphology.

Given the intriguing nature of our experimental findings, a necessity arose for a theoretical exploration aimed at elucidating the underlying factors behind the observed signal inversion. Our primary focus was on investigating the impact of inter-molecular interactions on the resultant CD spectrum observed for increasing the surface coverage of L-cys. To address this, we conducted *ab initio* DFT calculations of the CD spectra of representative models of L-cys adsorbed on the Au(111) surface. Our objective is not to replicate the experimental observations but rather to explore the hypothesis that a switch in the CD signal can simply result from the introduction of intermolecular interactions as the concentration of L-cys on the surface of the nanoparticle increases. For this purpose, we employed a simple model. First, periodic models of L-cys adsorbed on gold (111) terminated slabs were constructed to simulate low and high coverage. Then, the geometrically optimized systems were cut into cluster models in order to perform the CD calculations.

To mimic the experimental conditions, we considered a (4 × 4) supercell 3-layer thick slab representing the (111) termination. Low coverage, corresponding to an experimental concentration of 0.9 μmol $L^{-1}$, included one L-cys molecule, whereas high coverage, corresponding to a concentration of 2.7 μmol $L^{-1}$ and higher, included 2 molecules. We used the geometries reported by López *et al.*,[21] who extensively investigated the adsorption behavior of L-cys on various gold surfaces. According to their work, the adsorption of a single L-cys molecule on the (111) gold surface reveals a preference for the zwitterionic form where L-cys exhibits both $[NH_3]^+$ and [COOH] fragments. At higher concentrations, inter-molecular interactions became apparent, characterized by the formation of a hydrogen bond of length 1.603 Å between two L-cys molecules.

Fig. 5 displays the periodic slab models optimized, together with the cluster models cut from them; the cluster structures were not subsequently re-optimized and are achiral as Fig. S13† shows a non-significant CD signal arising from the bare cluster. The cluster substrate has a composition of $Au_{64}$ and is also 3 atomic layers thick. Low coverage was modelled by one molecule and high coverage by 2 molecules in the interaction, named $Au_{64}$(L-cys) and $Au_{64}$(L-cys)$_2$, respectively. Special attention was paid to the positioning of L-cys to sit in the center of the metallic surface so as to not encounter side effects that could be a source of error in the CD calculations.

The calculated theoretical CD spectra reveal the presence of several peaks in the range of 500 and 700 nm. The peaks of the low concentration model are of lower intensity than those of the high concentration model, in line with the observations. More interestingly, a notable inversion in polarizability between 500 and 625 nm is observed (Fig. 6): whereas the low coverage model exhibits a positive Cotton effect around 525 and 580 nm, the high coverage spectrum exhibits the opposite behaviour. The same feature is clearly observed at the regions around 500 and 545 nm with a negative Cotton effect for the low concentration model and the opposite for the high coverage model. In the region higher than 625 nm, the correlation is less clear as the peaks for the two models do not appear in the same range.

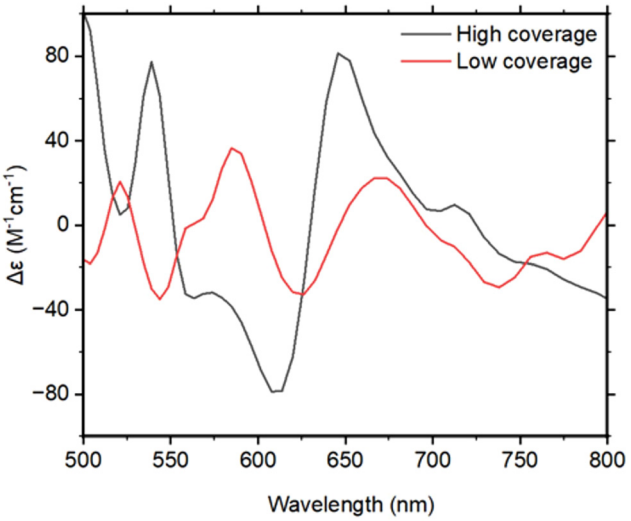


Fig. 6 Theoretical circular dichroism spectra of L-cys on Au surfaces for different coverages.

Overall, both the calculated and the obtained CD spectra display an inversion of the signal associated with the concentration of L-cys. This finding suggests that the incorporation of intermolecular interactions may play a crucial role in the observed chiroptical response of gold twisted nanoarrows. The physics behind the chiral behaviour of nanoparticles is complex and not fully understood. The CD signal depends both on the electric and magnetic dipoles (see eqn (1)). It seems thus reasonable to assume that the adsorption of a single molecule may induce a different electromagnetic response from the adsorption of neighboring molecules in

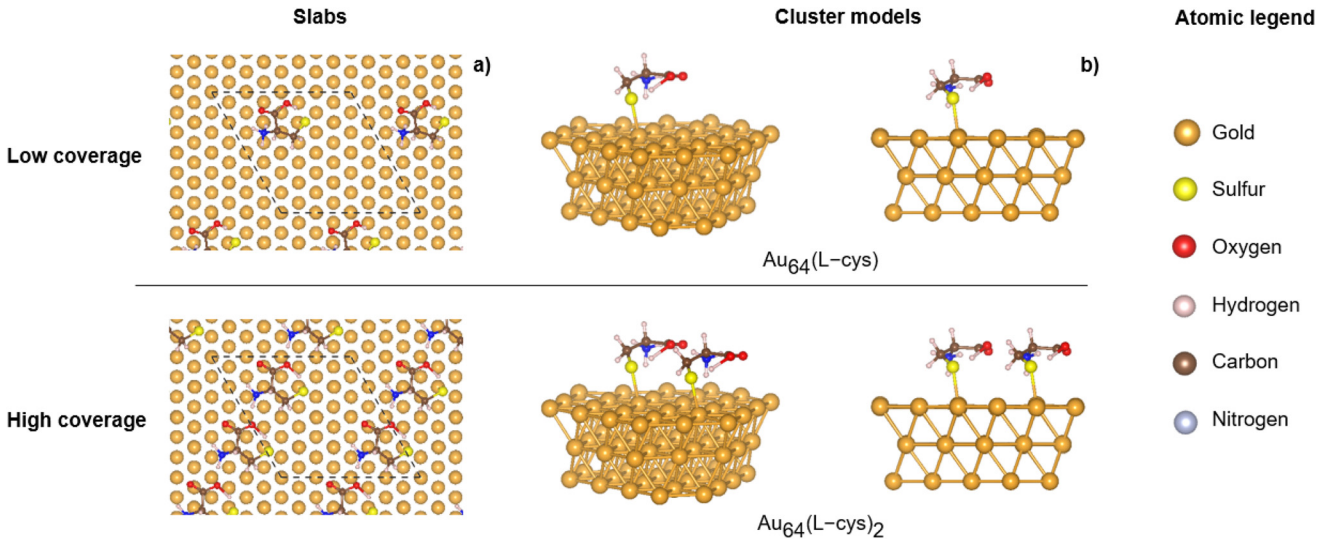


Fig. 5 Models used for the calculation of CD spectra: (a) most stable low- and high-coverage slab structures extracted from ref. 21; top view with the unit cell in dashed lines, and (b) different side views of the corresponding cluster models used for the calculation of circular dichroism spectra.

interaction, as the electronic rearrangement between the substrate and molecule(s) will be modified. This is in line with Govorov's theoretical work[20] and is also consistent with the observations of CD sign inversion when using different substrates.[51] Our results point to the intermolecular interactions between adsorbed chiral molecules as a plausible cause for the inversion in the dichroic response observed for L-cysteine and glutathione on gold twisted nanoarrows.

This outcome represents a step forward in understanding the chirality transfer mechanism during the fabrication of chiral gold NCs. Subsequent investigations are underway to provide a systematic and comprehensive physical/chemical explanation for this observed change in the CD sign.

## Conclusion

In summary, we report a synthetic route to obtain chiral plasmonic gold nanoarrows *via* a seed mediated route. We carried out a detailed investigation on how the morphology of the system changes with varying concentrations of L-cysteine in growth solution. Our results show clearly its important role in both the morphological distortion and the modulation of chiroplasmonic properties of gold nanocrystals. We observed that L-cysteine adsorbs preferentially on the (110) facets and that these facets progressively disappear leading to the (111) facets, by increasing the L-cysteine concentration in the growth solution. Spectroscopy measurements (circular dichroism and Raman) confirm that cysteine adsorption on gold surfaces is at the origin of the chirality transfer. Interestingly, we have also observed that the same enantiomer can cause an inversion of the signal of dichroism by the change in its concentration during the synthesis.

*Ab initio* (TD)-DFT calculations demonstrated that the adsorption of L-cysteine on gold (111) at different coverages results in the opposite behaviour of CD spectra, in line with the experimental observations. The differences in chiroplasmonic properties can be explained by intermolecular interactions between cysteine molecules on the gold surface.

## Author contributions

Nada Khalfaoui Hassani: investigation and writing. Ndeye Haby Awe: investigation. M. Tabut: formal analysis, software, and writing. Christophe Desmarets: validation and reviewing. Daniele Toffoli and Mauro Stener: methodology, software, and reviewing. Nicolas Goubet: validation and reviewing. Monica Calatayud: DFT supervision and reviewing. Caroline Salzemann: supervision and writing – original draft.

## Data availability

The following files are available in the ESI.† Fig. S1: Schematic representation of the seed-mediated growth of nanorods and nano-arrows. Fig. S2: Structural characterization of single crystalline gold nanorods obtained by the seeding process with CTAB and hydroquinone. Fig. S3: UV-visible spectra of the elongated seeds and nanoarrows in the absence of cysteine. Fig. S4: TEM images and UV-visible and CD spectra of nanoarrows obtained at different concentrations of cysteine from 0 to 9.1 μmol $L^{-1}$. Fig. S5: Raman spectra of nano-arrows obtained in the absence and in the presence of cysteine at different concentrations. Fig. S6: Circular dichroism spectra obtained with L/D-cysteine. Fig. S7: Structural characterization of nanoarrows obtained in the absence of cysteine. Fig. S8: Determination of the size, volume and surface of nanorods and nanoarrows from TEM images. Fig. S9: TEM and CD spectra of nanoarrows functionalized after synthesis from L-cysteine. Raman spectra before and after functionalization for low and high concentrations. Fig. S10: Kinetic UV-Visible spectra obtained during 240 min for low and high concentrations. Fig. S11: TEM images of extracted nanoparticles after 10, 30, 60 and 120 minutes of growth in the presence of 0.9 and 9.1 μmol $L^{-1}$ of cysteine. Fig. S12: CD and TEM images of nano-arrows obtained by seed-mediated growth in the presence of 0.9, 2.7 and 9.1 μmol $L^{-1}$ of glutathione. Fig. S13: Theoretical CD spectrum of the bare $Au_{64}$ cluster. The following theoretical calculations are available in the NOMAD repository (upload_name=CHIRNATIO - Cluster AMS): input and output files of the computed CD spectra for the two cluster models, as well as the optimized geometries of the periodic calculations. The experimental data are available in Recherche Data Gouv†.

## Conflicts of interest

There are no conflicts to declare.

## Acknowledgements

The authors thank Marc Petit, Marion Barbazanges and Vladimiro Mujica for fruitful discussions. Assia Hessani and Ludovic Bellot-Gurlet are acknowledged for their assistance with Raman spectroscopy measurements. This research was partly funded by the French National Research Agency (ANR) under the project ANR-22-CE09-0007. Initiative Sciences et Ingénierie Moléculaires-iSiM from Sorbonne Universite is warmly acknowledged for financial support. This work was performed using HPC resources from GENCI-IDRIS (Grant 2023-A0150802131). In the interest of open access publication, the author applies a CC-BY open access license to any article accepted for publication as a result of this submission.

## References

1 M. Schäferling, *Chiral Nanophotonics: Chiral Optical Properties of Plasmonic Systems*, Springer International Publishing, Cham, 2017, vol. 205.
2 A. Ben-Moshe, B. M. Maoz, A. O. Govorov and G. Markovich, *Chem. Soc. Rev.*, 2013, **42**, 7028.

3 M. J. Urban, C. Shen, X.-T. Kong, C. Zhu, A. O. Govorov, Q. Wang, M. Hentschel and N. Liu, *Annu. Rev. Phys. Chem.*, 2019, **70**, 275–299.
4 T. Liu, L. V. Besteiro, T. Liedl, M. A. Correa-Duarte, Z. Wang and A. O. Govorov, *Nano Lett.*, 2019, **19**, 1395–1407.
5 M. L. Solomon, A. A. E. Saleh, L. V. Poulikakos, J. M. Abendroth, L. F. Tadesse and J. A. Dionne, *Acc. Chem. Res.*, 2020, **53**, 588–598.
6 V. K. Valev, J. J. Baumberg, C. Sibilia and T. Verbiest, *Adv. Mater.*, 2013, **25**, 2517–2534.
7 W. Ma, L. Xu, A. F. de Moura, X. Wu, H. Kuang, C. Xu and N. A. Kotov, *Chem. Rev.*, 2017, **117**, 8041–8093.
8 J. T. Collins, C. Kuppe, D. C. Hooper, C. Sibilia, M. Centini and V. K. Valev, *Adv. Opt. Mater.*, 2017, **5**, 1700182.
9 Y. Xia, X. Xia and H.-C. Peng, *J. Am. Chem. Soc.*, 2015, **137**, 7947–7966.
10 A. Carone, P. Mariani, A. Désert, M. Romanelli, J. Marcheselli, M. Garavelli, S. Corni, I. Rivalta and S. Parola, *ACS Nano*, 2022, **16**, 1089–1101.
11 G. Zheng, J. He, V. Kumar, S. Wang, I. Pastoriza-Santos, J. Pérez-Juste, L. M. Liz-Marzán and K.-Y. Wong, *Chem. Soc. Rev.*, 2021, **50**, 3738–3754.
12 G. González-Rubio, J. Mosquera, V. Kumar, A. Pedrazo-Tardajos, P. Llombart, D. M. Solís, I. Lobato, E. G. Noya, A. Guerrero-Martínez, J. M. Taboada, F. Obelleiro, L. G. MacDowell, S. Bals and L. M. Liz-Marzán, *Science*, 2020, **368**, 1472–1477.
13 H.-E. Lee, H.-Y. Ahn, J. Mun, Y. Y. Lee, M. Kim, N. H. Cho, K. Chang, W. S. Kim, J. Rho and K. T. Nam, *Nature*, 2018, **556**, 360–365.
14 Y. Ma, Z. Cao, J. Hao, J. Zhou, Z. Yang, Y. Yang and J. Wei, *J. Phys. Chem. C*, 2020, **124**, 24306–24314.
15 N.-N. Zhang, H.-R. Sun, Y. Xue, F. Peng and K. Liu, *J. Phys. Chem. C*, 2021, **125**, 10708–10715.
16 X. Wen, S. Wang, R. Liu, R. Duan, S. Hu, T. Jiao, L. Zhang and M. Liu, *Small*, 2022, **18**, 2104301.
17 B. Ni, M. Mychinko, S. Gómez-Graña, J. Morales-Vidal, M. Obelleiro-Liz, W. Heyvaert, D. Vila-Liarte, X. Zhuo, W. Albrecht, G. Zheng, G. González-Rubio, J. M. Taboada, F. Obelleiro, N. López, J. Pérez-Juste, I. Pastoriza-Santos, H. Cölfen, S. Bals and L. M. Liz-Marzán, *Adv. Mater.*, 2023, **35**, 2208299.
18 A. O. Govorov, Z. Fan, P. Hernandez, J. M. Slocik and R. R. Naik, *Nano Lett.*, 2010, **10**, 1374–1382.
19 A. O. Govorov, *J. Phys. Chem. C*, 2011, **115**, 7914–7923.
20 A. O. Govorov and Z. Fan, *ChemPhysChem*, 2012, **13**, 2551–2560.
21 J. Morales-Vidal, N. López and M. A. Ortuño, *J. Phys. Chem. C*, 2019, **123**, 13758–13764.
22 D. Toffoli, A. Russi, G. Fronzoni, E. Coccia, M. Stener, L. Sementa and A. Fortunelli, *J. Phys. Chem. Lett.*, 2021, **12**, 5829–5835.
23 H. Portalés, N. Goubet, S. Casale, X. Z. Xu, M. Ariane, A. Mermet, J. Margueritat and L. Saviot, *ACS Nano*, 2020, **14**, 4395–4404.
24 G. Kresse and J. Furthmüller, *Comput. Mater. Sci.*, 1996, **6**, 15–50.
25 G. Kresse and J. Furthmüller, *Phys. Rev. B:Condens. Matter Mater. Phys.*, 1996, **54**, 11169.
26 P. E. Blöchl, *Phys. Rev. B:Condens. Matter Mater. Phys.*, 1994, **50**, 17953.
27 J. P. Perdew, K. Burke and M. Ernzerhof, *Phys. Rev. Lett.*, 1996, **77**, 3865.
28 M. Rosa, S. Corni and R. Di Felice, *Phys. Rev. B:Condens. Matter Mater. Phys.*, 2014, **90**, 125448.
29 S. Grimme, J. Antony, S. Ehrlich and H. Krieg, *J. Chem. Phys.*, 2010, **132**, 154104.
30 H. J. Monkhorst and J. D. Pack, *Phys. Rev. B*, 1976, **13**, 5188.
31 K. Momma and F. Izumi, *J. Appl. Crystallogr.*, 2011, **44**, 1272–1276.
32 O. Baseggio, G. Fronzoni and M. Stener, *J. Chem. Phys.*, 2015, **143**, 024106.
33 O. Baseggio, D. Toffoli, G. Fronzoni, M. Stener, L. Sementa and A. Fortunelli, *J. Phys. Chem. C*, 2016, **120**, 24335–24345.
34 E. Baerends, D. Ellis and P. Ros, *Chem. Phys.*, 1973, **2**, 41–51.
35 G. te Velde, F. M. Bickelhaupt, E. J. Baerends, C. Fonseca Guerra, S. J. A. van Gisbergen, J. G. Snijders and T. Ziegler, *J. Comput. Chem.*, 2001, **22**, 931–967.
36 A. D. Becke, *J. Chem. Phys.*, 1993, **98**, 5648–5652.
37 P. J. Stephens, F. J. Devlin, C. F. Chabalowski and M. J. Frisch, *J. Phys. Chem.*, 1994, **98**, 11623–11627.
38 M. Medves, L. Sementa, D. Toffoli, G. Fronzoni, A. Fortunelli and M. Stener, *J. Chem. Phys.*, 2020, **152**, 184104.
39 P. D'Antoni, M. Medves, D. Toffoli, A. Fortunelli, M. Stener and L. Visscher, *J. Phys. Chem. A*, 2023, **127**, 9244–9257.
40 E. v. Lenthe, E.-J. Baerends and J. G. Snijders, *J. Chem. Phys.*, 1993, **99**, 4597–4610.
41 J. W. Kim, N. H. Cho, Y.-C. Lim, S. W. Im, J. H. Han and K. T. Nam, *Mater. Adv.*, 2021, **2**, 6988–6995.
42 L. Scarabelli, A. Sánchez-Iglesias, J. Pérez-Juste and L. M. Liz-Marzán, *J. Phys. Chem. Lett.*, 2015, **6**, 4270–4279.
43 A. Gole and C. J. Murphy, *Chem. Mater.*, 2004, **16**, 3633–3640.
44 D. K. Smith and B. A. Korgel, *Langmuir*, 2008, **24**, 644–649.
45 K. Park, L. F. Drummy, R. C. Wadams, H. Koerner, D. Nepal, L. Fabris and R. A. Vaia, *Chem. Mater.*, 2013, **25**, 555–563.
46 Y. Xu, L. Chen, X. Ye, X. Wang, J. Yu, Y. Zhao, M. Cao, Z. Xia, B. Sun and Q. Zhang, *Nano Res.*, 2017, **10**, 2146–2155.
47 M. J. Walsh, W. Tong, H. Katz-Boon, P. Mulvaney, J. Etheridge and A. M. Funston, *Acc. Chem. Res.*, 2017, **50**, 2925–2935.
48 W. Wang, I. Erofeev, P. Nandi, H. Yan and U. Mirsaidov, *Adv. Funct. Mater.*, 2021, **31**, 2008639.
49 Q. Wang, Z. Wang, Z. Li, J. Xiao, H. Shan, Z. Fang and L. Qi, *Sci. Adv.*, 2017, **3**, e1701183.
50 X. Sun, J. Yang, L. Sun, G. Yang, C. Liu, Y. Tao, Q. Cheng, C. Wang, H. Xu and Q. Zhang, *ACS Nano*, 2022, **16**, 19174–19186.
51 Y. Chen, J. Zheng, L. Zhang, S. Li, Y. Chen, K. K. Chui, W. Zhang, L. Shao and J. Wang, *ACS Nano*, 2024, **18**, 383–394.

 